HAL
open science

Wetland emission and atmospheric sink changes explain methane growth in 2020

Shushi Peng, Xin Lin, Rona L Thompson, Yi Xi, Gang Liu, Didier Hauglustaine, Xin Lan, Benjamin Poulter, Michel Ramonet, Marielle Saunois, et al.

To cite this version:

Shushi Peng, Xin Lin, Rona L Thompson, Yi Xi, Gang Liu, et al.. Wetland emission and atmospheric sink changes explain methane growth in 2020. Nature, 2022, 612 (7940), pp.477 - 482. 10.1038/s41586-022-05447-w . hal-03917691

HAL Id: hal-03917691

https://hal.science/hal-03917691v1

Submitted on 2 Jan 2023

HAL is a multi-disciplinary open access archive for the deposit and dissemination of scientific research documents, whether they are published or not. The documents may come from teaching and research institutions in France or abroad, or from public or private research centers.

L'archive ouverte pluridisciplinaire **HAL**, est destinée au dépôt et à la diffusion de documents scientifiques de niveau recherche, publiés ou non, émanant des établissements d'enseignement et de recherche français ou étrangers, des laboratoires publics ou privés.

Wetland emission and atmospheric sink changes explain methane growth in 2020

https://doi.org/10.1038/s41586-022-05447-w

Received: 25 January 2022

Accepted: 14 October 2022

Published online: 14 December 2022

Check for updates

Shushi Peng[1,2,3]✉, Xin Lin[4]✉, Rona L. Thompson[5], Yi Xi[1,2], Gang Liu[1,2], Didier Hauglustaine[4], Xin Lan[6,7], Benjamin Poulter[8], Michel Ramonet[4], Marielle Saunois[4], Yi Yin[9], Zhen Zhang[10], Bo Zheng[11,12] & Philippe Ciais[4,13]

Atmospheric methane growth reached an exceptionally high rate of 15.1 ± 0.4 parts per billion per year in 2020 despite a probable decrease in anthropogenic methane emissions during COVID-19 lockdowns[1]. Here we quantify changes in methane sources and in its atmospheric sink in 2020 compared with 2019. We find that, globally, total anthropogenic emissions decreased by 1.2 ± 0.1 teragrams of methane per year (Tg CH_4 yr^{-1}), fire emissions decreased by 6.5 ± 0.1 Tg CH_4 yr^{-1} and wetland emissions increased by 6.0 ± 2.3 Tg CH_4 yr^{-1}. Tropospheric OH concentration decreased by 1.6 ± 0.2 per cent relative to 2019, mainly as a result of lower anthropogenic nitrogen oxide (NO_x) emissions and associated lower free tropospheric ozone during pandemic lockdowns[2]. From atmospheric inversions, we also infer that global net emissions increased by 6.9 ± 2.1 Tg CH_4 yr^{-1} in 2020 relative to 2019, and global methane removal from reaction with OH decreased by 7.5 ± 0.8 Tg CH_4 yr^{-1}. Therefore, we attribute the methane growth rate anomaly in 2020 relative to 2019 to lower OH sink (53 ± 10 per cent) and higher natural emissions (47 ± 16 per cent), mostly from wetlands. In line with previous findings[3,4], our results imply that wetland methane emissions are sensitive to a warmer and wetter climate and could act as a positive feedback mechanism in the future. Our study also suggests that nitrogen oxide emission trends need to be taken into account when implementing the global anthropogenic methane emissions reduction pledge[5].

Methane (CH_4) contributes 15–35% of the increase in radiative forcing from greenhouse gases emitted by human activities[6]. The atmospheric methane growth rate (MGR) has been high over the past decade, probably owing to the combined increases in fossil fuel and microbial sources[7–11]. In 2020, the MGR observed from surface sites of the NOAA Global Monitoring Laboratory (GML) network reached 15.1 ± 0.4 parts per billion per year (ppb yr^{-1}), the highest value from 1984 to 2020 (Extended Data Fig. 1)[12]. The MGR was larger in the Northern than in the Southern Hemisphere, which suggests at first glance an increase of northern sources (Fig. 1). A similar, abnormally large, growth rate of 14.8 ppb yr^{-1} was also detected from total column concentration measurements (XCH_4) by the Greenhouse Gases Observing Satellite (GOSAT; Supplementary Fig. 1). In the same year, the coronavirus pandemic led to a strong reduction of fossil fuel use, probably accompanied by a drop of CH_4 emissions by 10% from oil and gas extraction, according to reports from the International Energy Agency (IEA)[1] and regional estimates of emissions over extraction basins, such as the Permian Basin[13]. The reduced combustion of carbon fuels[14] and lower fire emissions[15] also caused less carbon monoxide (CO) and nitrogen oxides (NO_x) to be released to the atmosphere during the first half of 2020[16,17]. Both CO and NO_x affect the atmospheric concentration of the hydroxyl radical (OH), which is the main sink of CH_4. Even a small change in OH has a large impact on the MGR[8]. Meanwhile, the atmospheric CH_4 concentration also feeds back on the OH available to remove air pollutants such as CO and NO_x (refs. [18,19]). Reduced CO emissions should increase the concentration of OH, whereas reduced NO_x emissions should decrease OH (ref. [5]), except in very polluted areas[20]. Thus, the net effect of COVID-19 emission changes on the MGR is uncertain. In addition, the year 2020 was exceptionally hot from early spring to late summer over northern Eurasia, a sensitive region for CH_4 emissions from biogenic sources such as wetlands, permafrost slumps and arctic lakes, which are expected to emit more CH_4 as the temperature increases. Determining whether the high MGR anomaly in 2020 was due to less atmospheric removal resulting from a decrease in OH or to enhanced biogenic sources is key to developing our understanding of the complex interplay of the anthropogenic and natural drivers of

[1]Sino-French Institute for Earth System Science, College of Urban and Environmental Sciences, Peking University, Beijing, China. [2]Laboratory for Earth Surface Processes, Peking University, Beijing, China. [3]Institute of Carbon Neutrality, Peking University, Beijing, China. [4]Laboratoire des Sciences du Climat et de l'Environnement, LSCE/IPSL, CEA-CNRS-UVSQ, Université Paris-Saclay, Gif-sur-Yvette, France. [5]Norwegian Institute for Air Research (NILU), Kjeller, Norway. [6]Cooperative Institute for Research in Environmental Sciences of University of Colorado, Boulder, CO, USA. [7]Global Monitoring Laboratory, National Oceanic and Atmospheric Administration, Boulder, CO, USA. [8]Biospheric Sciences Laboratory, NASA Goddard Space Flight Center, Greenbelt, MD, USA. [9]Division of Geological and Planetary Sciences, California Institute of Technology, Pasadena, CA, USA. [10]Department of Geographical Sciences, University of Maryland, College Park, MD, USA. [11]Institute of Environment and Ecology, Tsinghua Shenzhen International Graduate School, Tsinghua University, Shenzhen, China. [12]State Environmental Protection Key Laboratory of Sources and Control of Air Pollution Complex, Beijing, China. [13]Climate and Atmosphere Research Center (CARE-C), The Cyprus Institute, Nicosia, Cyprus. ✉e-mail: speng@pku.edu.cn; xinlin.res@gmail.com

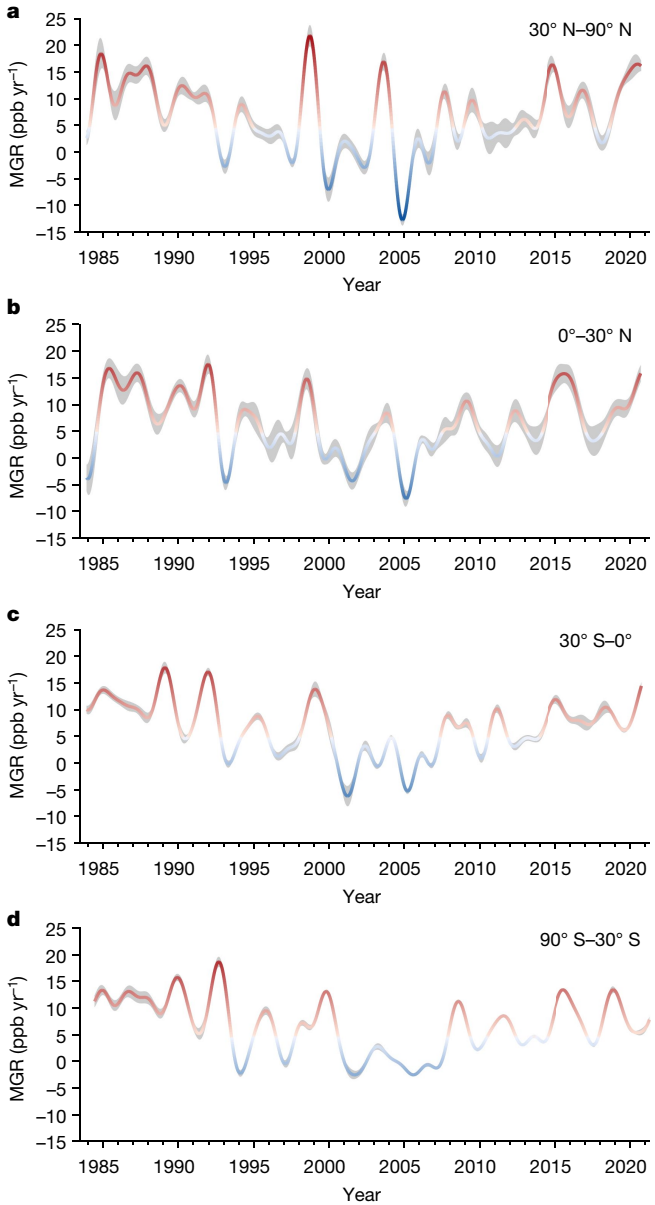

Fig. 1 | Atmospheric MGRs of four latitudinal bands. a–d, The annual growth rate is derived from weekly average marine surface atmospheric methane concentrations at NOAA's surface sites in the four latitudinal bands following a previous work[45]. The colours correspond to the annual growth rate: warm colours for higher growth rate and cool colours for lower growth rate. The grey shaded area shows the standard deviation of the annual growth rate.

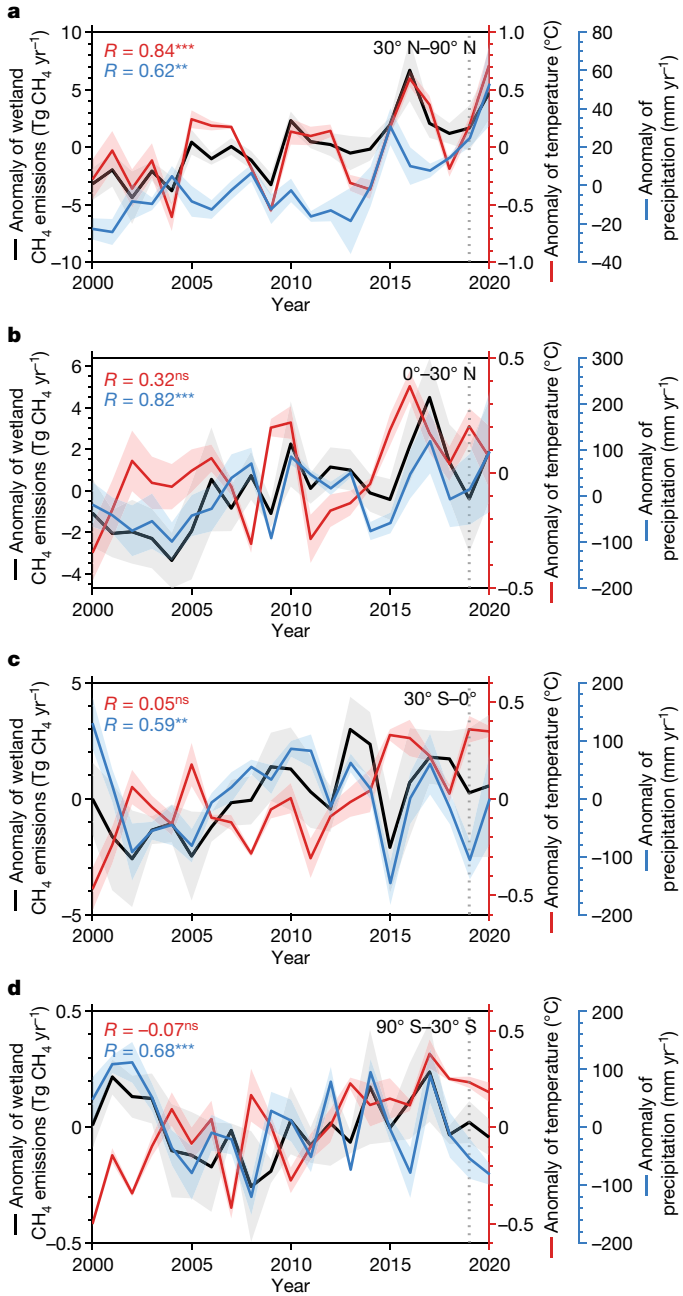

Fig. 2 | Wetland methane emissions and temperature and precipitation in the four latitudinal bands during the period 2000–2020. a–d, The black lines show the anomalies of average wetland emissions simulated from the two WEMs with four climate forcing. The temperature anomalies over wetlands, from CRU TSv4.05, ERA5 and MERRA2, and the precipitation anomalies over wetlands, from these three datasets and MSWEP, are shown in red and blue, respectively. The shaded area shows the standard deviation of 12 simulations for wetland emissions (eight from ORCHIDEE-MICT and four from LPJ-wsl, see Methods). The correlation coefficients between wetland emissions and temperature (red) and precipitation (blue) are also marked in the upper left of each panel, with *** for $P < 0.001$, ** for $P < 0.01$ and ns for not significant. The vertical dashed line marks the year of 2019 for reference.

the methane budget required for the upcoming Global Stocktake of the Paris Agreement. Here we combined bottom-up and top-down approaches to understand the high MGR anomaly in 2020 relative to 2019 and quantified anomalies in the surface sources and in the global atmospheric OH sink.

A bottom-up view of emission anomalies

First, we estimated the change in anthropogenic CH_4 emissions in 2020 from the fossil fuel, agriculture and waste sectors. To do so, we combined national greenhouse gas inventories (NGHGIs) submitted to the United Nations (UN) Framework Convention on Climate Change (UNFCCC) for Annex-I countries and the updated Emissions Database for Global Atmospheric Research (EDGAR) v6.0 inventory[21] with new activity data from IEA[22] and the Food and Agriculture Organization (FAO)[23] of the UN for other countries (see Methods). In the category of fossil fuel extraction activities, global coal production decreased by 4.6% in 2020 compared with 2019, and global oil production and natural gas production decreased by 7.9% and 3.8%, respectively[22]. We inferred a decrease of CH_4 emissions from oil and natural gas (−3.1 Tg CH_4 yr^{-1}) and from coal mining (−1.3 Tg CH_4 yr^{-1}). In the agricultural sector,

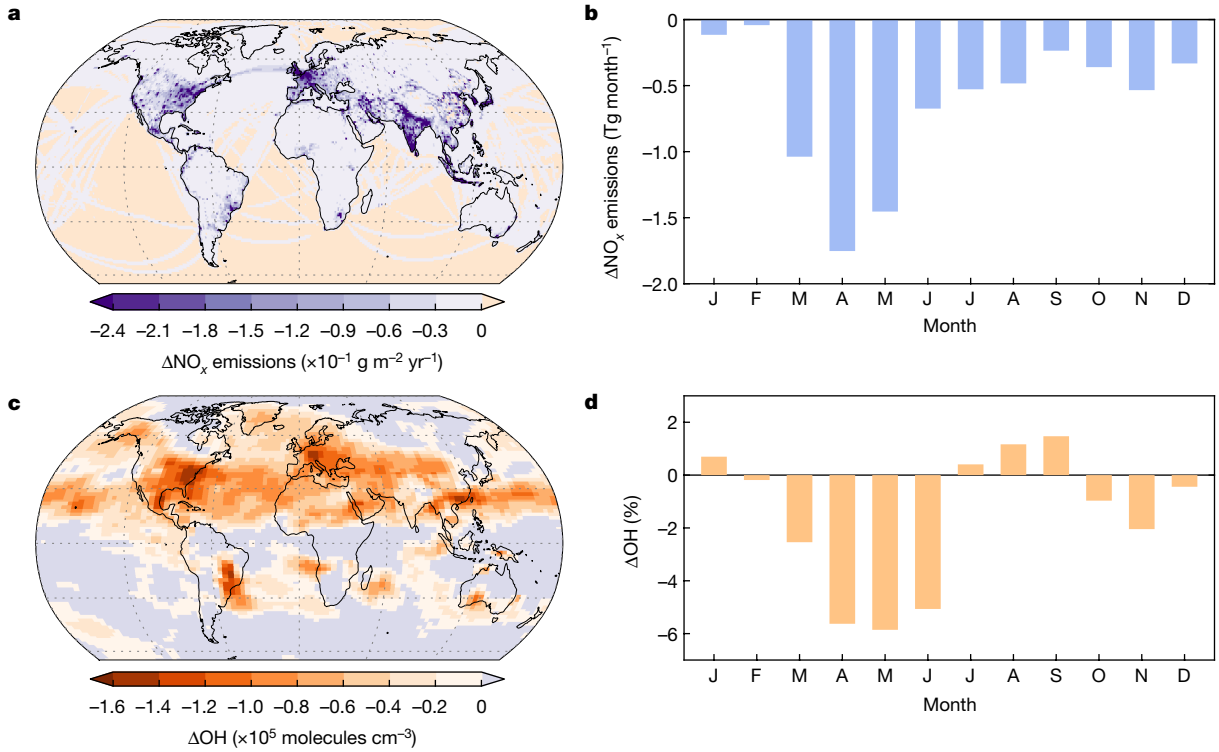

Fig. 3 | Anomaly of NO_x emissions and tropospheric hydroxyl radical (OH) in 2020 relative to 2019. a,**c**, Spatial patterns of NO_x emissions anomaly (ΔNO_x emissions; **a**) and OH anomaly (ΔOH; **c**) in 2020 relative to 2019. **b**,**d**, Difference in monthly global NO_x emissions (**b**) and monthly tropospheric OH (**d**) between 2020 and 2019. The NO_x emissions data are from the Community Emissions Data System dataset[36].

the global rice cultivation area slightly increased according to FAO[23] by 1% (+0.5 Tg CH_4 yr^{-1}), and an increase in livestock stock and slaughter numbers was reported as well (+1.6 Tg CH_4 yr^{-1}). Statistical data are not yet available for the waste sector for non-Annex-I countries, so we used the linear trends from EDGAR v6.0 for 2014–2018 to project a small global increase of +1.0 Tg CH_4 yr^{-1} in 2020 compared with 2019. In summary, the anthropogenic CH_4 emissions in 2020 decreased by 1.2 ± 0.1 Tg CH_4 yr^{-1} (± standard deviation, hereinafter) (Extended Data Fig. 2), which at steady state would lead only to a 0.4 ± 0.0 ppb yr^{-1} decrease of growth in the atmosphere relative to 2019, based on the conversion factor of 2.75 Tg CH_4 ppb^{-1} (ref. [24]). This shows that the observed MGR anomaly of 5.2 ± 0.7 ppb yr^{-1} in 2020 compared with 2019 (15.1 ± 0.4 ppb yr^{-1} of MGR in 2020 relative to 9.9 ± 0.6 ppb yr^{-1} of MGR in 2019) must be attributed to a change of natural emissions and/or OH sink.

We then estimated biogenic and fire CH_4 emissions in 2020 from bottom-up models. The year 2020 was wetter than normal in northern and tropical regions (Supplementary Fig. 2), and extremely warm in northern Eurasia from early spring to late summer[25] (Extended Data Fig. 3). Two satellite-based fire emission datasets, the Global Fire Assimilation System (GFAS) and the Global Fire Emissions Database (GFED4.1s), consistently show that the global fire emissions in 2020 were lower by 6.5 ± 0.1 Tg CH_4 yr^{-1} than in 2019 (Extended Data Fig. 4). The southern tropical regions (30° S–0°) dominated the 2020 decrease in fire emissions in both datasets, although in the USA there were fewer fires in the first half of the year but more in the second half of the year[26]. The GFAS data show that eastern Siberia had higher fire emissions in 2020 compared with 2019, by 0.4 Tg CH_4 yr^{-1}. This anomaly is related to the heatwave in the region (Extended Data Fig. 3)[25], where the fire season advanced by two months in 2020 and began in May[27]. Globally, fire emissions appear to have dropped in 2020 compared with 2019, implying other processes must explain the large positive MGR anomaly in 2020.

We found that most wetland areas of the world were exposed to warmer and wetter conditions in 2020 than normal years (Fig. 2 and Extended Data Fig. 3). Northern wetlands were exposed to warmer temperatures (+0.43–0.58 °C) relative to 2019 as shown in Fig. 2 (Supplementary Table 1). Precipitation over global wetlands[28] had a 2–11% annual increase relative to 2019, mainly in the northern high latitudes and in the tropics (Supplementary Table 1). With increased precipitation, an expansion of wetland area and more shallow water tables promoting emissions are expected. In addition, the earlier soil thaw and later soil freeze in 2020 resulted in a longer emission season in the high northern wetlands (Supplementary Fig. 3), and possibly in increased emissions from permafrost and thermokarst lakes. To quantify wetland emissions from 2000 to 2020, we used two process-based wetland emission models (WEMs) forced by different climate datasets (see Methods). These models show that wetland emissions significantly and positively correlate with precipitation in the tropics (30° S–30° N)[29] and in the southern extra-tropics (90° S–30° S) and with both temperature and precipitation in northern wetlands (30° N–90° N) (Fig. 2). Warmer and wetter wetlands over the Northern Hemisphere in 2020 (Supplementary Table 1) increased emissions by 6.0 ± 2.5 Tg CH_4 yr^{-1} relative to 2019, dominating the net increase in global wetland emissions (6.0 ± 2.3 Tg CH_4 yr^{-1}) in 2020 (Extended Data Fig. 5). The spread in the estimates of WEMs is mainly due to differences in wetland area related to differences in the precipitation forcing (Supplementary Fig. 2), and partly to model structure, even though the two models have similarities in parameterizations. With a 4% increase in precipitation over wetlands from the Multi-Source Weighted-Ensemble Precipitation (MSWEP) precipitation field, which merges gauge, satellite, and reanalysis data to obtain accurate precipitation estimates[30,31], wetland emissions increased by 5.8 ± 1.5 Tg CH_4 yr^{-1}. Using root-zone soil moisture from Global Land Evaporation Amsterdam Model (GLEAM) v3.5a[32] as a proxy to calculate the expansion of wetland areas in 2020 (see Methods), we found a larger wetland emission increase of 7.4–9.3 Tg CH_4 yr^{-1}, mainly in the Northern Hemisphere (Extended Data Fig. 5). Observed land liquid water mass change from the GRACE-FO satellite[33] confirms

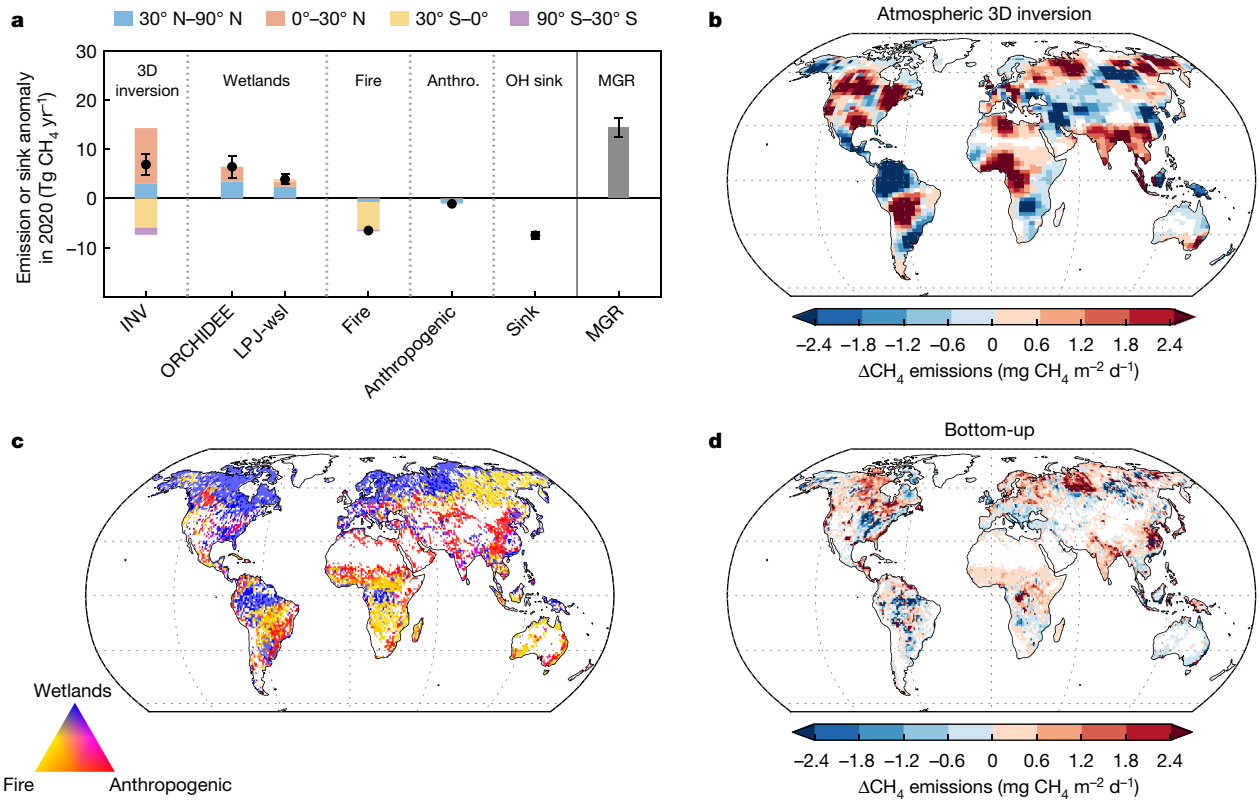

Fig. 4 | Methane emissions and sink anomaly in 2020 relative to 2019. **a**, Methane emissions anomaly of four latitudinal bands derived from atmospheric 3D inversions with OH field from LMDZ-INCA simulations (INV), wetland emissions anomaly from two WEMs, fire emissions anomaly from GFED4.1s and GFAS, and anthropogenic (Anthro.) emissions anomaly. The black dots show the net changes in global CH_4 emissions between 2020 and 2019. The sink anomaly is calculated by a 1.6 ± 0.2% decrease in OH in INV. The observed MGR anomaly (14.4 ± 2.0 Tg CH_4 yr^{-1}) from surface sites is defined as the difference in MGR between 2020 (15.1 ± 0.4 ppb yr^{-1}) and 2019 (9.9 ± 0.6 ppb yr^{-1}) with a conversion factor of 2.75 Tg CH_4 ppb^{-1}. The error bars represent one standard deviation. **b**, Spatial pattern of emissions anomaly from top-down INV. **c**, Spatial distribution of contribution sources (wetlands, fire and anthropogenic) to change in emissions derived from bottom-up estimates. **d**, Spatial pattern of emissions anomaly from bottom-up estimates including wetland, fire and anthropogenic emissions.

that wetlands water storage increased in the Northern Hemisphere. The increase in soil moisture over wetlands in the Northern Hemisphere simulated by the two WEMs is less than the liquid mass change observed from GRACE-FO, especially north of 30° N (Supplementary Figs. 4 and 5), suggesting that the expansion of Northern Hemisphere wetlands or the water table levels—and thus emissions in 2020—may be underestimated by WEMs. Overall, it is probable that wetland emissions made a dominant contribution to the soaring level of atmospheric methane in 2020, although there is uncertainty regarding the magnitude of the contribution, mainly owing to uncertainty in the precipitation data.

According to our ensemble of bottom-up estimates, an increase in wetland emissions (6.0 ± 2.3 Tg CH_4 yr^{-1}) does not fully explain the increased methane emissions (14.4 ± 2.0 Tg CH_4 yr^{-1}) inferred from the MGR anomaly (5.2 ± 0.7 ppb yr^{-1}) between 2020 and 2019 under the assumption that the sink remains unchanged. Considering a decrease in anthropogenic emissions of 1.2 Tg CH_4 yr^{-1} and fire emissions of 6.5 Tg CH_4 yr^{-1}, even with our largest estimate of wetland emissions (9.4 Tg CH_4 yr^{-1}), the bottom-up budget is still not closed, revealing a missing source anomaly of more than 12.7 Tg CH_4 yr^{-1}, which must be attributed to a decrease in the atmospheric CH_4 sink, to additional sources such as lakes or permafrost or to extra-wetland emissions that were missed by the WEMs.

Atmospheric constraints in 2020

The increase in wetland emissions is mainly located in the Northern Hemisphere, whereas the decrease in fire emissions is mainly in southern tropical regions, and so we expect that the MGR in the Northern Hemisphere should be higher than the MGR in the Southern Hemisphere. Indeed, the latitudinal averaged growth rate of methane observed from the surface sites confirms that the Northern Hemisphere had a higher growth rate than the Southern Hemisphere in 2020 (Supplementary Fig. 6). The GOSAT data, which provide an MGR integrated over the whole column, and are thus much less sensitive to changes in the depth of the boundary layer at continental stations, also show a similar latitudinal pattern to the data from the surface sites, with a peak in the column growth rate at 10° N–50° N (Supplementary Fig. 7).

To quantify the spatial and temporal distribution of emission anomalies in 2020 from atmospheric observations, we used a three-dimensional (3D) atmospheric inversion assimilating surface CH_4 observations from a total of 103 stations (see Methods). Inversions have the advantage over bottom-up methods to match the observed MGR and gradients between all stations. We performed a 3Datmospheric inversion (INV) that prescribes changes in the OH concentration field, as simulated by a full chemistry transport model (LMDZ-INCA)[34,35] with realistic CO, hydrocarbons and NO_x anthropogenic emissions derived from gridded near-real-time fossil fuel combustion data that include lockdown-induced reductions in 2020[36,37]. The chemistry transport model is driven by meteorology from ECMWF ERA5 data[38] and biomass burning emissions from GFED4.1s[15]. Figure 3 shows a decrease in NO_x emissions by 6% in 2020 relative to 2019, which is particularly apparent in the spring (March, April and May) when COVID-19 lockdown measures were imposed in many Northern Hemisphere countries (Extended Data Fig. 6). The decrease in global NO_x emissions in 2020 relative to 2019

was seven times larger than the decreasing trend from 2005 to 2019 (Supplementary Figs. 8 and 9). Both the global NO_x emissions and satellite-derived tropospheric NO_2 concentration from Ozone Monitoring Instrument (OMI) in 2020 were the lowest during the period 2005–2020 (Supplementary Fig. 9). Our chemistry transport model LMDZ-INCA produced a globally averaged 1.6% decrease in annual tropospheric OH concentration in 2020 relative to 2019. The decrease in monthly tropospheric OH reached as high as 6% in April, May and June (Fig. 3d) over the Northern Hemisphere (0°–60° N; Extended Data Fig. 7), suggesting that the drop of NO_x emissions in 2020 outweighed the effects of a decrease in anthropogenic and fire CO emissions (Supplementary Fig. 10) and made OH lower. To independently verify this modelled decrease of global OH in 2020, we used a 12-box model to infer changes in OH[9,39] by simultaneously optimizing OH concentration and the emissions of two HFC and one HCFC species (HCFC-141b, HFC-32 and HFC-134a) using atmospheric observations of these three species from the NOAA and AGAGE networks including the latest data for 2020. This diagnostic of OH is based on the premise that errors in the prior emissions should be largely independent between the three gases, but errors in OH will be correlated for all of them (see Methods). The box model shows a net decrease in OH of 1.6–1.8% in 2020 relative to 2019 after the optimization. This estimate of the OH decrease in 2020 is independent and consistent with the full chemistry model simulation.

Prescribed with the decrease of OH and its spatial pattern from the chemistry transport model, the INV gives a global increase of 6.9 ± 2.1 Tg CH_4 yr^{-1} for surface emissions and a decrease of 7.5 ± 0.8 Tg CH_4 yr^{-1} for the weaker atmospheric CH_4 sink. Considering the uncertainty of the decrease in OH and of the observed MGR[12], the global increase in surface emissions and decrease in the atmospheric CH_4 sink contributed, respectively, 47 ± 16% and 53 ± 10% of the total positive MGR anomaly in 2020 relative to 2019 (Fig. 4). The global increase of surface emissions is decomposed into an increase in the Northern Hemisphere of 14.3 Tg CH_4 yr^{-1}, partly offset by a decrease in the Southern Hemisphere of 7.4 Tg CH_4 yr^{-1} (Fig. 4a). The spatial pattern of emission anomalies produced by INV confirms enhanced emissions in northern North America, and western and eastern Siberia hinted by the bottom-up wetland models. In the Northern Hemisphere, our maximum bottom-up estimate of the increase in wetland emissions (11.2 Tg CH_4 yr^{-1}) is, however, smaller than the solution of INV. This suggests that either wetland models underestimated emissions, possibly because of underestimated soil water content (see above), too deep water table, missed emissions from small wetlands and/or other sources spatially collocated with northern wetlands such as lake and pond emissions[40], aquaculture emissions[41] and thawing permafrost slump emissions[42]. The largest temperature anomaly of the past two decades was also indeed found over permafrost regions in 2020, particularly in Russia (Extended Data Fig. 3a and Supplementary Fig. 11), which could have increased methane emissions from upland permafrost soils[43] and lakes, including thermokarst lakes[44]. Estimation of changes in emissions from lakes (including reservoirs) and permafrost shows limited contributions from these two sources (<0.1 Tg CH_4 yr^{-1}) to fill the gap in the emission changes between bottom-up and top-down approaches, although with large uncertainties (Supplementary Information). We note that owing to the sparse atmospheric networks in Central and South Asia, Middle East, Africa and tropical South America (Supplementary Fig. 12), the inferred fluxes and therefore flux changes in these regions may have large uncertainties. The evaluations against independent observations revealed that emission changes over large latitudinal bands or at hemispheric scales are robustly constrained (Supplementary Figs. 13–18). In addition, an extension of our 3D inversion and analyses to cover the period 2015–2020 also showed similar attribution of the MGR anomaly in 2020 (Supplementary Fig. 19).

In summary, our results show that an increase in wetland emissions, owing to warmer and wetter conditions over wetlands, along with decreased OH, contributed to the soaring methane concentration in 2020. The large positive MGR anomaly in 2020, partly due to wetland and other natural emissions, reminds us that the sensitivity of these emissions to interannual variation in climate has had a key role in the renewed growth of methane in the atmosphere since 2006. The wetland methane–climate feedback is poorly understood, and this study shows a high interannual sensitivity that should provide a benchmark for future coupled CH_4 emissions–climate models. We also show that the decrease in atmospheric CH_4 sinks, which resulted from a reduction of tropospheric OH owing to less NO_x emissions during the lockdowns, contributed 53 ± 10% of the MGR anomaly in 2020 relative to 2019. Therefore, the unprecedentedly high methane growth rate in 2020 was a compound event with both a reduction in the atmospheric CH_4 sink and an increase in Northern Hemisphere natural sources. With emission recovery to pre-pandemic levels in 2021, there could be less reduction in OH. The persistent high MGR anomaly in 2021 hints at mechanisms that differ from those responsible for 2020, and thus awaits an explanation. Our study highlights that future improvements in air quality with reduced NO_x emissions may increase the lifetime of methane in the atmosphere[5], and therefore would require more reduction of methane emissions to achieve the target of Paris Agreement.

Online content

Any methods, additional references, Nature Portfolio reporting summaries, source data, extended data, supplementary information, acknowledgements, peer review information; details of author contributions and competing interests; and statements of data and code availability are available at https://doi.org/10.1038/s41586-022-05447-w.

1. International Energy Agency (IEA). *Methane Tracker 2021* (accessed 1 May 2022); https://www.iea.org/reports/methane-tracker-2021.
2. Miyazaki, K. et al. Global tropospheric ozone responses to reduced NO_x emissions linked to the COVID-19 worldwide lockdowns. *Sci. Adv.* **7**, eabf7460 (2021).
3. Koffi, E. N., Bergamaschi, P., Alkama, R. & Cescatti, A. An observation-constrained assessment of the climate sensitivity and future trajectories of wetland methane emissions. *Sci. Adv.* **6**, eaay4444 (2020).
4. Zhang, Z. et al. Emerging role of wetland methane emissions in driving 21st century climate change. *Proc. Natl Acad. Sci. USA* **114**, 9647–9652 (2017).
5. Laughner, J. L. et al. Societal shifts due to COVID-19 reveal large-scale complexities and feedbacks between atmospheric chemistry and climate change. *Proc. Natl Acad. Sci. USA* **118**, e2109481118 (2021).
6. IPCC & Masson-Delmotte, V. et al. (eds). *Climate Change 2021: The Physical Science Basis. Contribution of Working Group I to the Sixth Assessment Report of the Intergovernmental Panel on Climate Change* (Cambridge Univ. Press, 2021).
7. Jackson, R. B. et al. Increasing anthropogenic methane emissions arise equally from agricultural and fossil fuel sources. *Environ. Res. Lett.* **15**, 071002 (2020).
8. Turner, A. J., Frankenberg, C. & Kort, E. A. Interpreting contemporary trends in atmospheric methane. *Proc. Natl Acad. Sci. USA* **116**, 2805–2813 (2019).
9. Thompson, R. L. et al. Variability in atmospheric methane from fossil fuel and microbial sources over the last three decades. *Geophys. Res. Lett.* **45**, 11499–11508 (2018).
10. Worden, J. R. et al. Reduced biomass burning emissions reconcile conflicting estimates of the post-2006 atmospheric methane budget. *Nat. Commun.* **8**, 2227 (2017).
11. Yin, Y. et al. Accelerating methane growth rate from 2010 to 2017: leading contributions from the tropics and East Asia. *Atmos. Chem. Phys.* **21**, 12631–12647 (2021).
12. Lan, X., Thoning, K. W. & Dlugokencky, E. J. *Trends in Atmospheric Methane* (NOAA, accessed 1 May 2022); https://gml.noaa.gov/ccgg/trends_ch4.
13. Lyon, D. R. et al. Concurrent variation in oil and gas methane emissions and oil price during the COVID-19 pandemic. *Atmos. Chem. Phys.* **21**, 6605–6626 (2021).
14. Friedlingstein, P. et al. Global Carbon Budget 2021. *Earth Syst. Sci. Data* **14**, 1917–2005 (2022).
15. van der Werf, G. R. et al. Global fire emissions estimates during 1997–2016. *Earth Syst. Sci. Data* **9**, 697–720 (2017).
16. Cooper, M. J. et al. Global fine-scale changes in ambient NO_2 during COVID-19 lockdowns. *Nature* **601**, 380–387 (2022).
17. Zheng, B. et al. Satellite-based estimates of decline and rebound in China's CO_2 emissions during COVID-19 pandemic. *Sci. Adv.* **6**, eabd4998 (2020).
18. Nguyen, N. H., Turner, A. J., Yin, Y., Prather, M. J. & Frankenberg, C. Effects of chemical feedbacks on decadal methane emissions estimates. *Geophys. Res. Lett.* **47**, e2019GL085706 (2020).
19. Shindell, D. et al. Simultaneously mitigating near-term climate change and improving human health and food security. *Science* **335**, 183–189 (2012).
20. Zhu, Q., Laughner, J. L. & Cohen, R. C. Estimate of OH trends over one decade in North American cities. *Proc. Natl Acad. Sci. USA* **119**, e2117399119 (2022).
21. Crippa, M. et al. *GHG Emissions of All World Countries: 2021 Report* (Publications Office of the European Union, 2021); https://doi.org/10.2760/173513.
22. International Energy Agency. *World Energy Balances: Overview* (IEA, accessed 1 May 2022); https://www.iea.org/reports/world-energy-balances-overview/world.

23. Food and Agriculture Organization of the United Nations (FAO). *FAOSTAT Emissions Land Use Database* (FAO, accessed 1 May 2022); https://www.fao.org/faostat/en/#data.
24. Prather, M. J., Holmes, C. D. & Hsu, J. Reactive greenhouse gas scenarios: systematic exploration of uncertainties and the role of atmospheric chemistry. *Geophys. Res. Lett.* **39**, L09803 (2012).
25. Overland, J. E. & Wang, M. The 2020 Siberian heat wave. *Int. J. Climatol.* **41**, E2341–E2346 (2021).
26. Poulter, B., Freeborn, P. H., Jolly, W. M. & Varner, J. M. COVID-19 lockdowns drive decline in active fires in southeastern United States. *Proc. Natl Acad. Sci. USA* **118**, e2105666118 (2021).
27. Witze, A. The Arctic is burning like never before — and that's bad news for climate change. *Nature* **585**, 336–337 (2020).
28. Tootchi, A., Jost, A. & Ducharne, A. Multi-source global wetland maps combining surface water imagery and groundwater constraints. *Earth Syst. Sci. Data* **11**, 189–220 (2019).
29. Feng, L., Palmer, P. I., Zhu, S., Parker, R. J. & Liu, Y. Tropical methane emissions explain large fraction of recent changes in global atmospheric methane growth rate. *Nat. Commun.* **13**, 1378 (2022).
30. Beck, H. E. et al. MSWEP: 3-hourly 0.25° global gridded precipitation (1979–2015) by merging gauge, satellite, and reanalysis data. *Hydrol. Earth Syst. Sci.* **21**, 589–615 (2017).
31. Beck, H. E. et al. MSWEP V2 Global 3-Hourly 0.1° precipitation: methodology and quantitative assessment. *B. Am. Meteorol. Soc.* **100**, 473–500 (2019).
32. Martens, B. et al. GLEAM v3: satellite-based land evaporation and root-zone soil moisture. *Geosci. Model Dev.* **10**, 1903–1925 (2017).
33. Landerer, F. W. et al. Extending the global mass change data record: GRACE Follow-On instrument and science data performance. *Geophys. Res. Lett.* **47**, e2020GL088306 (2020).
34. Hauglustaine, D. A. et al. Interactive chemistry in the Laboratoire de Météorologie Dynamique general circulation model: description and background tropospheric chemistry evaluation. *J. Geophys. Res. Atmos.* **109**, D04314 (2004).
35. Hauglustaine, D. A., Balkanski, Y. & Schulz, M. A global model simulation of present and future nitrate aerosols and their direct radiative forcing of climate. *Atmos. Chem. Phys.* **14**, 11031–11063 (2014).
36. Community Emissions Data System (CEDS). *CEDS v_2021_04_21 Gridded Emissions Data* (PNNL, accessed 1 July 2021); https://data.pnnl.gov/dataset/CEDS-4-21-21.
37. *Carbon Monitor* (accessed 1 July 2021); https://carbonmonitor.org.
38. Hersbach, H. et al. ERA5 hourly data on single levels from 1980 to present. (Copernicus Climate Change Service, Climate Data Store, accessed 1 May 2021); https://doi.org/10.24381/cds.adbb2d47.
39. Cunnold, D. M. et al. In situ measurements of atmospheric methane at GAGE/AGAGE sites during 1985–2000 and resulting source inferences. *J. Geophys. Res. Atmos.* **107**, ACH 20-1–ACH 20-18 (2002).
40. Rosentreter, J. A. et al. Half of global methane emissions come from highly variable aquatic ecosystem sources. *Nat. Geosci.* **14**, 225–230 (2021).
41. Yuan, J. et al. Rapid growth in greenhouse gas emissions from the adoption of industrial-scale aquaculture. *Nat. Clim. Change* **9**, 318–322 (2019).
42. Kuhn, M. A. et al. Opposing effects of climate and permafrost thaw on CH_4 and CO_2 emissions from northern lakes. *AGU Advances* **2**, e2021AV000515 (2021).
43. Zona, D. et al. Cold season emissions dominate the Arctic tundra methane budget. *Proc. Natl Acad. Sci. USA* **113**, 40–45 (2016).
44. Schuur, E. A. G. et al. Climate change and the permafrost carbon feedback. *Nature* **520**, 171–179 (2015).
45. Dlugokencky, E. J., Steele, L. P., Lang, P. M. & Masarie, K. A. The growth rate and distribution of atmospheric methane. *J. Geophys. Res. Atmos.* **99**, 17021–17043 (1994).

Publisher's note Springer Nature remains neutral with regard to jurisdictional claims in published maps and institutional affiliations.

Springer Nature or its licensor (e.g. a society or other partner) holds exclusive rights to this article under a publishing agreement with the author(s) or other rightsholder(s); author self-archiving of the accepted manuscript version of this article is solely governed by the terms of such publishing agreement and applicable law.

© The Author(s), under exclusive licence to Springer Nature Limited 2022

Methods

Atmospheric methane growth rate (MGR)

We used the monthly time series of globally averaged marine surface atmospheric methane concentration covering the period July 1983–Dec 2020 from NOAA's Global Monitoring Laboratory (NOAA/GML)[12,45]. After the seasonal cycle of atmospheric methane is removed by the CCGvu programme[46], the smoothed annual MGR shown in Fig. 1a is the MGR calculated for each specific month (for example, 1 March in that year to 1 March of the next year). The annual MGR in a given year is the increase in its abundance (mole fraction) from 1 January in that year to 1 January of the next year[12]. The MGR anomaly in 2020 relative to 2019 is defined as the difference in MGR between 2020 (15.1 ± 0.4 ppb yr^{-1}) and 2019 (9.9 ± 0.6 ppb yr^{-1}).

Anthropogenic methane emissions

For Annex-I countries that reported their national greenhouse gas inventories (NGHGIs) to UNFCCC and updated to 2020, we used the reported anthropogenic emissions (coal mining, oil and gas production, agriculture and waste) of these 41 countries (https://unfccc.int/ghg-inventories-annex-i-parties/2022). For other countries, emissions from coal mining, oil and gas production, agriculture and waste from 2000 to 2018 were from EDGAR v6.0[21]. We collected updated activity data from IEA[22] and FAO[23] for 2019 and 2020, and used the same emission factors as 2018 from EDGAR v6.0 to estimate methane emissions from coal mining, oil and gas production and agriculture sources in 2019 and 2020. For oil and gas production and combustion, we collected data from IEA[22]. For coal production, we collected coal production data from IEA[22] and corrected China's production using data from the statistical yearbook for China[47]. For agricultural activity data, we used livestock data and rice cultivation area from FAO[23]. As waste activity data are not yet available for these countries, we used the linear trends of waste sector from EDGAR v6.0 for 2014–2018 to project the change in 2020 relative to 2019.

Global fire methane emissions

Both the Global Fire Emissions Database version 4.1 including small fire burned area (GFED4.1s)[15] and the Global Fire Assimilation System (GFAS, https://atmosphere.copernicus.eu/global-fire-monitoring) from Copernicus Atmosphere Monitoring Service (CAMS) are used to derive monthly global fire methane emissions. GFED4.1s combines satellite information on fire activity and vegetation productivity to estimate the gridded monthly burned area and fire emissions, and has a spatial resolution of 0.25° × 0.25° (ref. [15]). Note that GFED4.1s fire emissions in 2017 and 2020 are from the beta version. The GFAS assimilates fire radiative power (FRP) observations from satellites to produce daily estimates of biomass burning emissions. We aggregated the GFAS daily fire emissions into monthly emissions.

Wetland CH_4 emissions simulated by models

We used two process-based WEMs to simulate global wetland CH_4 emissions: ORCHIDEE-MICT[48] and LPJ-wsl[4]. These two WEMs simulate methane production and transport to the atmosphere through diffusion, ebullition and plant transportation based on a previously published framework[49]. To estimate the uncertainty of the change in wetland emissions in 2020, four climate forcing datasets were used to drive the two WEMs. First, we downloaded two reanalysis climate datasets: hourly ERA5 with a spatial resolution of 0.25° × 0.25° from 1979 to 2020[38] and hourly MERRA2 with a spatial resolution of 0.5° × 0.625° from 1980 to 2020[50]. We resampled these two reanalysis datasets (air temperature, precipitation, humidity, downward shortwave and longwave radiation, surface air pressure and wind speed) into 1° × 1° and 0.5° × 0.5° resolutions to drive ORCHIDEE-MICT and LPJ-wsl, respectively. These different climate datasets had large differences in the change of precipitation in 2020 (Supplementary Fig. 2), so we also used monthly temperature and precipitation data from CRU TS v4.05[51] and monthly precipitation from MSWEP v2.8[30,31] to calibrate the ERA5 climate forcing. For the CRU data, we added the difference in monthly temperature between CRU and ERA5 into the hourly ERA5 temperature field, and scaled the ratio of monthly precipitation between CRU and ERA5 into hourly ERA5 precipitation from 1979 to 2020. These scaled data, along with the other unchanged ERA5 fields, were used to drive the models. For the MSWEP precipitation data, we only scaled the ratio of monthly precipitation between MSWEP and ERA5 into hourly ERA5 precipitation, and these data along with the other ERA5 fields was used to drive the models. The wetland area dynamics were simulated by a TOPMODEL-based diagnostic model that has successfully predicted the spatial distribution and seasonality of natural wetlands extents (dynamics by ORCHIDEE-MICT[52] and dynamics by LPJ-wsl[53] are described previously). For wetland dynamics simulated in ORCHIDEE-MICT, two wetland maps were used to calibrate the parameters, one is the Regularly Flooded Wetlands static map (RFW)[28] recording the long-term maximum wetland area used to calibrate the long-term maximum wetland extent for each grid cell, and the other is the satellite-based global inundation product GIEMS-2 (Global Inundation Estimate from Multiple Satellites version 2)[54] used to calibrate the yearly maximum wetland extent for each grid cell. Details of wetland dynamics and the parameter calibration can be found in earlier works[52,55]. Thus, for wetland emissions simulated by ORCHIDEE-MICT, we obtained two sets of wetland dynamics for each climate forcing: in total, eight simulations with four climate forcing and two sets of calibrated parameters from RFW and GIEMS2. In addition, we also used monthly root zone soil moisture from GLEAM v3.5a products[32] with TOPMODEL to calculate wetland area dynamics, and with wetland emission density per wetland area from ORCHIDEE-MICT plus ERA5 climate forcing, we derived an additional estimate of the change in wetland emissions in 2020.

AGAGE 12-box model and inversions

This model has four equal area boxes in the latitudinal direction (90° N–30° N, 30° N–0°, 0°–30° S, 30° S–90° S) and three boxes in the vertical representing the lower and upper troposphere, and stratosphere, and has been used extensively in atmospheric chemistry and lifetime studies[39,56,57]. Horizontal and vertical mixing rates between the boxes are provided monthly and are based on a climatology of empirical values. The model was integrated in two-day time steps using the fourth-order vectorized Runge–Kutta algorithm. Atmospheric chemistry is calculated at each time step using Arrhenius equations and includes OH reactions. Atmospheric inversions were performed using the adjoint of the AGAGE 12-box model and a quasi-Newton algorithm to find the best linear unbiased estimate (for details see a previous work)[9].

OH was optimized by simultaneously solving for an annual scalar of OH concentration and the monthly emissions of two HFC species (HFC-134a and HFC-32) and HCFC-141b, on the basis of the premise that errors in the prior emissions of these species are probably not strongly correlated, whereas the impact of errors in the prior OH on the atmospheric concentrations of all three species will be fully correlated. The three species were chosen because they all are principally lost by oxidation by OH, have relatively short atmospheric lifetimes (14, 5.4 and 9.4 years for HFC-134a, HFC-32 and HCFC-141b, respectively) and have had substantial emissions over the past decade[58]. Observations were used from the NOAA GML discrete sampling network, which has 12 sites globally with observation uncertainties of 0.2 ppt, 0.2 ppt and 0.1 ppt for the mean concentrations in the four latitudinal boxes for HFC-134a, HFC-32 and HCFC-141b, respectively. Prior emissions of HFC-134a and HFC-32 were based on UNFCCC reports and published data[59] for China with seasonality based on ref. [60]. Prior emissions of HCFC-141b were from ref. [58]. Uncertainties of the two HFC species were based on previous estimates[59] and for HCFC-141b an uncertainty of 50% was assumed. Prior OH concentrations were obtained from the Copernicus reanalysis product EAC4[61]. With the prior emission uncertainties described above

and 10% prior uncertainty for OH concentration, the decrease in OH in 2020 relative to 2019 was 1.8%, and the posterior uncertainty of OH decreased by 55% compared with the prior uncertainty. We ran another sensitivity test using 10% prior uncertainty for OH and 25% uncertainty in the prior emissions of all species, and found a 1.6% decrease in OH in 2020. An additional sensitivity test was run using a 5% prior uncertainty for the OH concentration, although it is too optimistic, and we found 0.6% decrease in OH in 2020. The inversed magnitude of change in OH partly depends on the prior uncertainties of OH and F gases, but still offers OH change signal from independent F-gases observations. The posterior uncertainty in OH was estimated as the 1 standard deviation (1σ) of the results from a Monte Carlo ensemble of 100 inversions, with random errors added to the prior emissions and observations for each member of the ensemble.

OH concentrations simulated from a full chemistry transport model LMDZ-INCA

Global gridded OH concentrations were simulated by the full chemistry transport model LMDZ-INCA[34,35]. The anthropogenic emissions were derived from the Community Emissions Data System (CEDS) emission inventory up to 2019[36] and were further updated to 2020 on the basis of the sectoral CO_2 emission changes estimated by Carbon Monitor[37] to reflect the influence of COVID-19 on emission changes. The emissions data revealed the decline and rebound in anthropogenic emissions of NO_x, the key precursor of OH, during and after the COVID-19 lockdowns around the world, which are broadly consistent with different bottom-up and top-down estimates[17,62,63]. For the baseline simulations, each year, we used the monthly anthropogenic emissions compiled previously[64]. These emissions include the different sectors: energy, industrial, residential, transportation and waste. The agricultural soil emissions for NO_x and NH_3 are also included, and no natural soil emissions are added in complement to those emissions. The biomass burning emissions are from GFED4.1s[15]. The ORCHIDEE vegetation model is used to calculate offline the biogenic surface fluxes of isoprene, terpenes, acetone and methanol as described previously[65]. Natural emissions of dust and sea salt are computed using the 10-m wind components from ECMWF ERA5 reanalysis. The lightning NO_x emissions are parameterized in the model on the basis of convective cloud heights as described in an earlier work[66]. On the basis of this parameterization, the total lightning NO_x emissions for the baseline simulation are 5.5 Tg N yr^{-1}. The meteorological fields used to drive the LMDZ-INCA model simulations were derived from the ECMWF ERA5 reanalysis dataset[38]. Our LMDZ-INCA simulations reproduced the monthly changes in mid-troposphere ozone and tropospheric NO_2 columns during the last decade up to 2020 (Supplementary Figs. 20 and 21). Given that ozone and NO_x have important roles in OH sources and sinks, the agreement of our LMDZ-INCA simulations with their observed values suggests that the simulations are representative of the global atmospheric chemical state including the variations of OH.

Atmospheric 3D inversion

A variational Bayesian inversion system, PYVAR-LMDZ-SACS, was used to infer weekly CH_4 fluxes at a spatial resolution of 1.9° (in latitude) by 3.75° (in longitude) between July 2018 and May 2021. The system combines a variational data assimilation system Python Variational (PYVAR)[67], an atmospheric transport model Laboratoire de Météorologie Dynamique with zooming capability (LMDZ)[68], and a Simplified Atmospheric Chemistry System (SACS)[69]. It has been widely applied to optimize sources and sinks of reactive atmospheric tracers such as CH_4 and CO[11,70–73], and has contributed to top-down inversions of the global CH_4 budgets[74,75]. Technically, the inversion system finds the optimal state vector that statistically best fits both the observations $\mathbf{y}$ and a prior state vector $\mathbf{x}^b$ weighted by their respective uncertainties (defined as the covariance matrices B and R), through iteratively minimizing a cost function J defined as follows:

$$J(\mathbf{x}) = 0.5(\mathbf{x}-\mathbf{x}^b)^T B^{-1}(\mathbf{x}-\mathbf{x}^b) + 0.5(H(\mathbf{x})-\mathbf{y})^T R^{-1}(H(\mathbf{x})-\mathbf{y}) \quad (1)$$

where $\mathbf{x}$ is the state vector that contains the variables to be optimized, including (1) the time series of grid-point-based eight-day mean surface emission fluxes of CH_4, and (2) grid-point-based scaling factors for the initial column-mean concentrations of CH_4. H represents the observation operator that projects the state vector into the observation space, and includes the chemistry-transport model (CTM) plus the convolution operation. Here, the CTM is composed of the atmospheric transport model LMDZ[68] coupled with the SACS module[69] that accounts for the chemical interactions between CH_4 and OH. The transport model was nudged towards reanalysed horizontal wind fields from ERA5, and run in an offline mode with precomputed three-hourly transport mass fluxes. The minimization of the cost function is solved iteratively until a reduction of 99% in the gradient of the cost function is achieved.

The prior CH_4 fluxes were compiled from existing bottom-up inventories for different sectors. Detailed information is given in Supplementary Table 2. The dataset incorporates recent development of emission inventories and current understanding of various CH_4 sources and sinks, and has therefore been proposed for use as the priors for top-down CH_4 inversions contributing to the next phase of the global methane budget assessment. The OH and $O(^1D)$ fields were prescribed from model outputs of the chemistry–climate model LMDZ-INCA with a full tropospheric photochemistry scheme[34,76] (see Methods section 'OH concentrations simulated from a full chemistry transport model LMDZ-INCA'). The definition of prior errors (the B matrix) follows previous schemes[11,70,71], that is, 70% for gridded CH_4 emissions.

Observations of CH_4 concentrations were obtained from ground-based greenhouse gas monitoring networks. For the set-up of observation constraints, surface in situ and flask–air CH_4 observations from a total of 103 stations were assimilated, including 71 stations with their records extending to late 2020 or early 2021, mostly from the NOAA and ICOS networks (Supplementary Fig. 12). All these observations have been reported on, or linked to, the WMOX2004 calibration scale. With respect to continuous CH_4 measurements, daily afternoon means (12:00–16:00 LST; LST, local sidereal time) were assimilated for stations below 1,000 m above sea level (a.s.l.) and morning means (0:00–4:00 LST) for those above 1,000 m a.s.l., owing to uncertainties in the model's representation of boundary layer mixing and complex terrain mesoscale circulations[77,78]. The observation errors (the R matrix) combine measurement errors, representation errors and transport model errors that contribute to model–observation misfits. For surface CH_4 observations, the synoptic variability at each station was used as a proxy for representation errors and transport model errors[70,71], and was calculated as the residual standard deviation (RSD) of the de-trended and de-seasonalized observations. For the effect of OH variations on derived emission anomalies, we took the OH field simulated by a full chemistry transport model LMDZ-INCA (see Methods section 'OH concentrations simulated from a full chemistry transport model LMDZ-INCA'). Note that, to ensure the assumption of OH changes from LMDZ-INCA, the OH fields were not adjusted in 3D inversions.

To validate the robustness of our 3D CH_4 inversion, we compared the prior and posterior model states with independent observations from multiple platforms (Supplementary Fig. 13), including the XCH_4 observations from the Total Carbon Column Observing Network (TCCON; Supplementary Figs. 14 and 15) and the CH_4 vertical profiles from aircraft samplings (Supplementary Fig. 16) and AirCore campaigns (Supplementary Figs. 17 and 18). The evaluation demonstrates the overall good performance of our 3D inversion in separating latitudinal emissions and representing large-scale atmospheric mixing (horizontally and vertically). The underestimation of XCH_4 increases in northern TCCON sites (Supplementary Figs. 14 and 15), as well as biases in the vertical CH_4 difference within northern low-to-mid latitudes (Supplementary Fig. 16), may suggest uncertainties in flux inversion

in the Northern Hemisphere, including those related to sparse data coverage (as shown in Supplementary Fig. 12 for certain regions) and inherent transport model errors (for example, biases in representing stratospheric processes) that are not resolved yet by the current model community.

Reporting summary

Further information on research design is available in the Nature Portfolio Reporting Summary linked to this article.

Data availability

All observation and model data that support the findings of this study are available as follows. The atmospheric methane growth rate data were obtained from https://gml.noaa.gov/ccgg/trends_ch4. The GOSAT satellite data were obtained from https://data2.gosat.nies.go.jp/. The EDGAR v6.0 data were downloaded from https://edgar.jrc.ec.europa.eu/country_profile. The hourly ERA5 reanalysis data were downloaded from https://www.ecmwf.int/en/forecasts/dataset/ecmwf-reanalysis-v5. The precipitation data from MERRA2 were downloaded from https://gmao.gsfc.nasa.gov/reanalysis/MERRA-2. The monthly temperature and precipitation data from CRU TS v4.05 were downloaded from https://crudata.uea.ac.uk/cru/data/hrg/cru_ts_4.05. The monthly precipitation from MSWEP v2.8 was downloaded from http://www.gloh2o.org/mswep. The GLEAM v3.5a root-zone soil moisture data were downloaded from https://www.gleam.eu. The RFW datasets are available at https://doi.org/10.1594/PANGAEA.892657. The land liquid water equilibrium from the GRACE-FO satellite was downloaded from https://gracefo.jpl.nasa.gov/data/grace-fo-data. The Global Fire Emissions Database version 4.1, including small fire burned area, was obtained from https://www.geo.vu.nl/~gwerf/GFED/GFED4. The monthly global fire methane emissions from the Global Fire Assimilation System (GFAS) from Copernicus Atmosphere Monitoring Service (CAMS) were obtained from https://apps.ecmwf.int/datasets/data/cams-gfas. The anthropogenic emissions from the CEDS emission inventory up to 2019 were downloaded from https://data.pnnl.gov/dataset/CEDS-4-21-21. The gridded near-real-time fossil fuel combustion data that include lockdown-induced reductions in 2020 were obtained from https://carbonmonitor.org. The tropospheric NO_2 concentration data from OMI satellite measurements were downloaded from https://disc.gsfc.nasa.gov/datasets/OMNO2_003/summary. The NOAA and ICOS surface CH_4 observations used in inversions are available at https://doi.org/10.15138/VNCZ-M766 and https://doi.org/10.18160/KCYX-HA35, respectively; surface CH_4 observations from other networks are available from the World Data Centre for Greenhouse Gases (https://gaw.kishou.go.jp) and the Global Environmental Database (https://db.cger.nies.go.jp/ged/en/index.html). The TCCON XCH_4 data were obtained from the TCCON Data Archive hosted by CaltechDATA at https://tccondata.org. The aircraft CH_4 vertical profiles are from NOAA's GGGRN (available at https://gml.noaa.gov/ccgg/obspack), IAGOS (available at https://www.iagos.org) and JMA (available at https://gaw.kishou.go.jp). The CH_4 measurements from NOAA's AirCore campaigns are publicly available at https://gml.noaa.gov/aftp/data/AirCore. The outputs of the two WEMs, LMDZ-INCA and atmospheric 3D inversions are publicly available at Figshare (https://doi.org/10.6084/m9.figshare.21076171). Source data are provided with this paper.

Code availability

Code and documentation for ORCHIDEE (MICT v8.4.4) is publicly available at http://forge.ipsl.jussieu.fr/orchidee. Code and documentation for the LPJ-wsl model is publicly available at https://github.com/benpoulter/LPJ-wsl_v2.0.git. The LMDZ-INCA global model is part of the Institut Pierre Simon Laplace (IPSL) Climate Modelling Center Coupled Model. The documentation on the code and the code itself can be found at https://cmc.ipsl.fr/ipsl-climate-models/ipsl-cm6.

46. Thoning, K. W., Tans, P. P. & Komhyr, W. D. Atmospheric carbon dioxide at Mauna Loa Observatory: 2. Analysis of the NOAA GMCC data, 1974–1985. *J. Geophys. Res. Atmos.* **94**, 8549–8565 (1989).
47. National Bureau of Statistics of China. *China Statistical Yearbook* (accessed 1 May 2021); http://www.stats.gov.cn/english/statisticaldata/annualdata.
48. Guimberteau, M. et al. ORCHIDEE-MICT (v8.4.1), a land surface model for the high latitudes: model description and validation. *Geosci. Model Dev.* **11**, 121–163 (2018).
49. Walter, B. P., Heimann, M. & Matthews, E. Modeling modern methane emissions from natural wetlands: 1. Model description and results. *J. Geophys. Res. Atmos.* **106**, 34189–34206 (2001).
50. Global Modeling and Assimilation Office (GMAO). *MERRA-2 tavg1_2d_flx_Nx: 2d,1-Hourly, Time-Averaged, Single-Level, Assimilation, Surface Flux Diagnostics V5.12.4* (Goddard Space Flight Center Distributed Active Archive Center (GSFC DAAC), accessed 1 April 2021); https://doi.org/10.5067/7MCPBJ41Y0K6.
51. Harris, I., Osborn, T. J., Jones, P. & Lister, D. Version 4 of the CRU TS monthly high-resolution gridded multivariate climate dataset. *Sci. Data* **7**, 109 (2020).
52. Xi, Y., Peng, S., Ciais, P. & Chen, Y. Future impacts of climate change on inland Ramsar wetlands. *Nat. Clim. Change* **11**, 45–51 (2021).
53. Zhang, Z., Zimmermann, N. E., Kaplan, J. O. & Poulter, B. Modeling spatiotemporal dynamics of global wetlands: comprehensive evaluation of a new sub-grid TOPMODEL parameterization and uncertainties. *Biogeosciences* **13**, 1387–1408 (2016).
54. Prigent, C., Jimenez, C. & Bousquet, P. Satellite-derived global surface water extent and dynamics over the last 25 years (GIEMS-2). *J. Geophys. Res. Atmos.* **125**, e2019JD030711 (2020).
55. Xi, Y. et al. Gridded maps of wetlands dynamics over mid-low latitudes for 1980–2020 based on TOPMODEL. *Sci. Data* **9**, 347 (2022).
56. Prinn, R. G. et al. Evidence for variability of atmospheric hydroxyl radicals over the past quarter century. *Geophys. Res. Lett.* **32**, L07809 (2005).
57. Rigby, M. et al. Renewed growth of atmospheric methane. *Geophys. Res. Lett.* **35**, L22805 (2008).
58. Simmonds, P. G. et al. Changing trends and emissions of hydrochlorofluorocarbons (HCFCs) and their hydrofluorocarbon (HFCs) replacements. *Atmos. Chem. Phys.* **17**, 4641–4655 (2017).
59. Lunt, M. F. et al. Reconciling reported and unreported HFC emissions with atmospheric observations. *Proc. Natl Acad. Sci. USA* **112**, 5927–5931 (2015).
60. Xiang, B. et al. Global emissions of refrigerants HCFC-22 and HFC-134a: unforeseen seasonal contributions. *Proc. Natl Acad. Sci. USA* **111**, 17379–17384 (2014).
61. Inness, A. et al. CAMS global reanalysis (EAC4) monthly averaged fields. (Copernicus Atmosphere Monitoring Service (CAMS) Atmosphere Data Store (ADS), accessed 1 June 2021); https://ads.atmosphere.copernicus.eu/cdsapp#!/dataset/cams-global-reanalysis-eac4-monthly.
62. Forster, P. M. et al. Current and future global climate impacts resulting from COVID-19. *Nat. Clim. Change* **10**, 913–919 (2020).
63. Lamboll, R. D. et al. Modifying emissions scenario projections to account for the effects of COVID-19: protocol for CovidMIP. *Geosci. Model Dev.* **14**, 3683–3695 (2021).
64. McDuffie, E. E. et al. A global anthropogenic emission inventory of atmospheric pollutants from sector- and fuel-specific sources (1970–2017): an application of the Community Emissions Data System (CEDS). *Earth Syst. Sci. Data* **12**, 3413–3442 (2020).
65. Messina, P. et al. Global biogenic volatile organic compound emissions in the ORCHIDEE and MEGAN models and sensitivity to key parameters. *Atmos. Chem. Phys.* **16**, 14169–14202 (2016).
66. Jourdain, L. & Hauglustaine, D. A. The global distribution of lightning NO_x simulated on-line in a general circulation model. *Phys. Chem. Earth Pt. C* **26**, 585–591 (2001).
67. Chevallier, F. et al. Inferring CO_2 sources and sinks from satellite observations: method and application to TOVS data. *J. Geophys. Res. Atmos.* **110**, D24309 (2005).
68. Hourdin, F. et al. The LMDZ4 general circulation model: climate performance and sensitivity to parametrized physics with emphasis on tropical convection. *Clim. Dynam.* **27**, 787–813 (2006).
69. Pison, I., Bousquet, P., Chevallier, F., Szopa, S. & Hauglustaine, D. Multi-species inversion of CH_4, CO and H_2 emissions from surface measurements. *Atmos. Chem. Phys.* **9**, 5281–5297 (2009).
70. Cressot, C. et al. On the consistency between global and regional methane emissions inferred from SCIAMACHY, TANSO-FTS, IASI and surface measurements. *Atmos. Chem. Phys.* **14**, 577–592 (2014).
71. Locatelli, R., Bousquet, P., Saunois, M., Chevallier, F. & Cressot, C. Sensitivity of the recent methane budget to LMDz sub-grid-scale physical parameterizations. *Atmos. Chem. Phys.* **15**, 9765–9780 (2015).
72. Zheng, B. et al. Global atmospheric carbon monoxide budget 2000–2017 inferred from multi-species atmospheric inversions. *Earth Syst. Sci. Data* **11**, 1411–1436 (2019).
73. Yin, Y. et al. Decadal trends in global CO emissions as seen by MOPITT. *Atmos. Chem. Phys.* **15**, 13433–13451 (2015).
74. Kirschke, S. et al. Three decades of global methane sources and sinks. *Nat. Geosci.* **6**, 813–823 (2013).
75. Saunois, M. et al. The Global Methane Budget 2000–2017. *Earth Syst. Sci. Data* **12**, 1561–1623 (2020).
76. Szopa, S. et al. Aerosol and ozone changes as forcing for climate evolution between 1850 and 2100. *Clim. Dynam.* **40**, 2223–2250 (2013).
77. Geels, C. et al. Comparing atmospheric transport models for future regional inversions over Europe – Part 1: mapping the atmospheric CO_2 signals. *Atmos. Chem. Phys.* **7**, 3461–3479 (2007).
78. Lin, X. et al. Simulating CH_4 and CO_2 over South and East Asia using the zoomed chemistry transport model LMDz-INCA. *Atmos. Chem. Phys.* **18**, 9475–9497 (2018).

Acknowledgements The study was supported by the National Natural Science Foundation of China (grant numbers 41722101 and 41830643). P.C. acknowledges support from the ESA CCI RECCAP2 project (ESRIN/4000123002/18/I-NB) and from the ANR CLand Convergence Institute. We are grateful to the many scientists and technicians for their contribution to the surface, aircraft, AirCore and TCCON CH_4 observations, and for their efforts in making these datasets available. This research is supported in part through computational resources provided by the High-performance Computing Platform of Peking University supercomputing facility and the Very Large Calculation Center (TGCC) of French Alternative Energies and Atomic Energy Commission (CEA), as well as the technical support from the IT team of LSCE.

Author contributions S.P., X. Lin and P.C. designed the study. G.L. and S.P. created the bottom-up anthropogenic emissions inventory. S.P. and Y.X. performed ORCHIDEE simulations; Z.Z. and B.P. performed LPJ-wsl simulations. D.H. and B.Z. performed LMDZ-INCA simulations, and R.L.T. performed AGAGE simulations. X. Lin performed atmospheric 3D inversions and model evaluation. M.R. and X. Lan provided surface CH_4 observations. S.P., Y.X. and X. Lin performed the analysis and created all the figures. S.P. drafted the manuscript, with substantial contributions from X. Lin and P.C. R.L.T., D.H., X. Lan., B.P., M.S., Y.Y., Z.Z. and B.Z. contributed to writing and commenting on the draft manuscript.

Competing interests The authors declare no competing interests.

Additional information

Supplementary information The online version contains supplementary material available at https://doi.org/10.1038/s41586-022-05447-w.

Correspondence and requests for materials should be addressed to Shushi Peng or Xin Lin.

Peer review information *Nature* thanks the anonymous reviewers for their contribution to the peer review of this work.

Reprints and permissions information is available at http://www.nature.com/reprints.

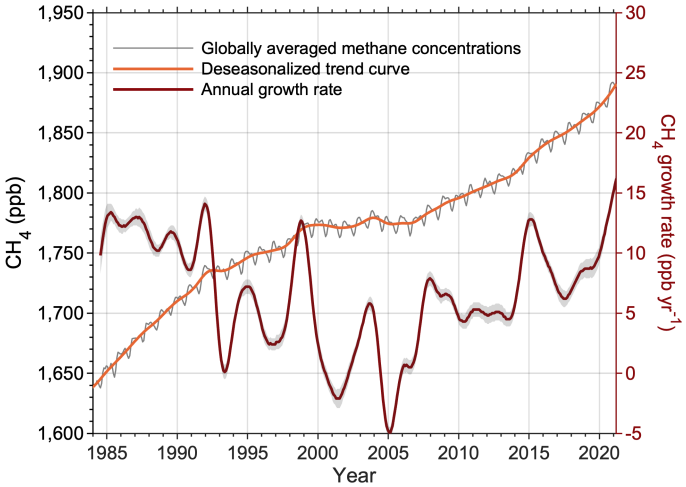

Extended Data Fig. 1 | Globally averaged methane concentrations and growth rates. Globally averaged monthly marine surface atmospheric methane concentrations from 1984 to 2020 from NOAA's Global Monitoring Laboratory (NOAA/GML, data available at https://gml.noaa.gov/ccgg/trends_ch4/)[12,45]. Orange line shows the trend curve with the seasonal cycle removed. Brown line shows annual growth rate, and grey shaded area shows the uncertainty of annual growth rate. Note that the uncertainties of global averaged methane concentration and deseasonalized trend are 0.6–3 ppm and 0.4–1.5 ppm, respectively.

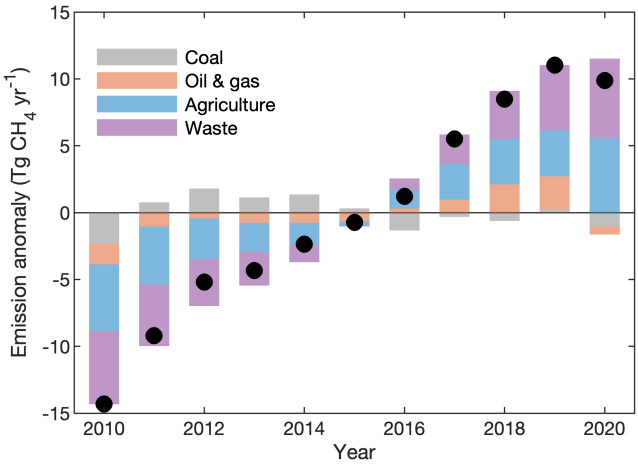

Extended Data Fig. 2 | Anthropogenic methane emissions from coal mining, oil and natural gas production, agriculture and waste. The black dots show anomaly of the total anthropogenic CH_4 emissions. For Annex-I countries, we used national greenhouse gas inventories (NGHGIs) submitted to UNFCCC (https://unfccc.int/ghg-inventories-annex-i-parties/2022). For other countries, we used EDGAR v6.0 covering the period 2010–2018, and updated to 2020 using activity data from IEA and FAO with constant emission factors from EDGAR v6.0.

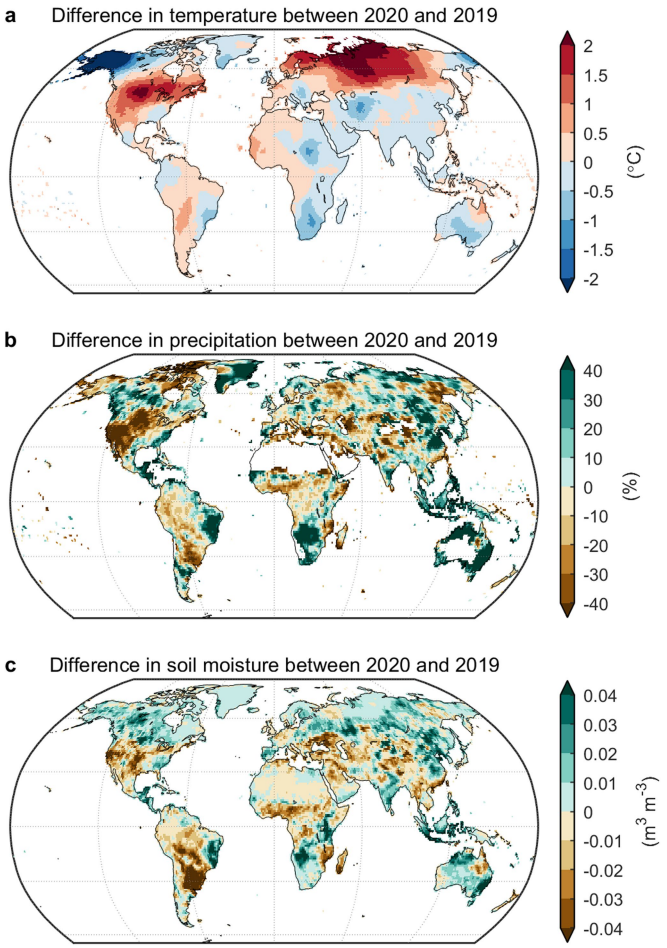

Extended Data Fig. 3 | Spatial patterns of difference in annual mean temperature, precipitation and soil moisture between 2020 and 2019. **a**, Annual mean temperature is from CRU TS v4.05 (https://crudata.uea.ac.uk/cru/data/hrg/cru_ts_4.05/). **b**, Annual precipitation is from MSWEP (http://www.gloh2o.org/mswep/). **c**, Annual mean soil moisture is from GLEAM v3.5a (https://www.gleam.eu/).

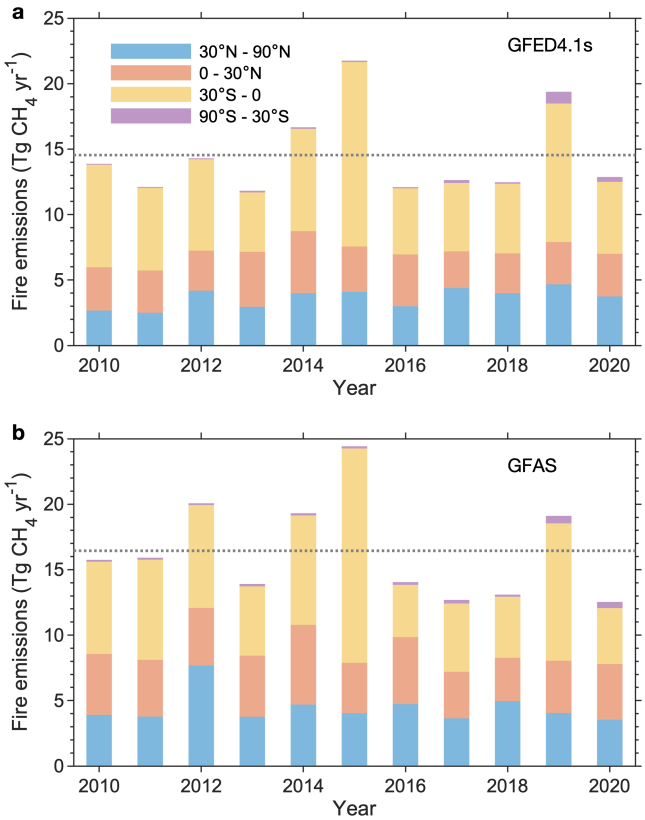

Extended Data Fig. 4 | Annual fire methane emissions from 2010 to 2020. **a**,**b**, Annual fire methane emissions derived from GFED4.1s (**a**) and GFAS (**b**) are shown for four latitudinal bands during the period 2010–2020. The horizontal dashed line indicates the average from 2010 to 2020. GFED4.1s is available at https://www.geo.vu.nl/~gwerf/GFED/GFED4/, and GFAS data are available at https://apps.ecmwf.int/datasets/data/cams-gfas/.

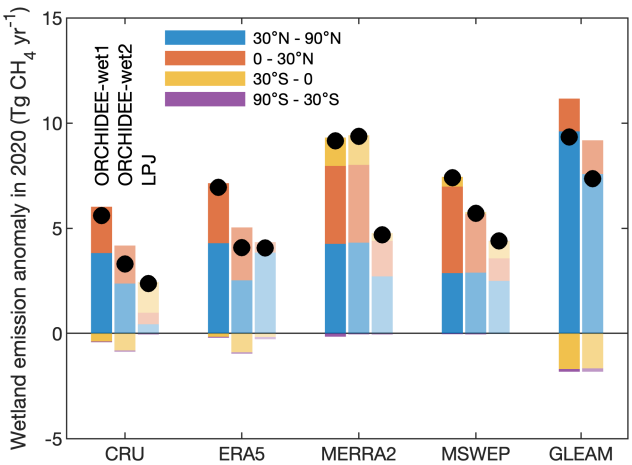

Extended Data Fig. 5 | Anomaly of wetland methane emissions in 2020 relative to 2019. Differences in wetland methane emissions between 2020 and 2019 are shown for four latitudinal bands from simulations of wetland emission models with different climate forcing data (CRU, ERA5, MERRA2 and MSWEP). ORCHIDEE-wet1 and ORCHIDEE-wet2 indicate that simulated wetland area dynamics are calibrated by RFW and GIEMS2, respectively. Note that changes in wetland emissions derived from wetland area calculated from GLEAM root zone soil moisture with CH_4 flux density per wetland area simulated from ERA5 are shown as "GLEAM" bars. The black dots show the anomaly of global wetland CH_4 emissions.

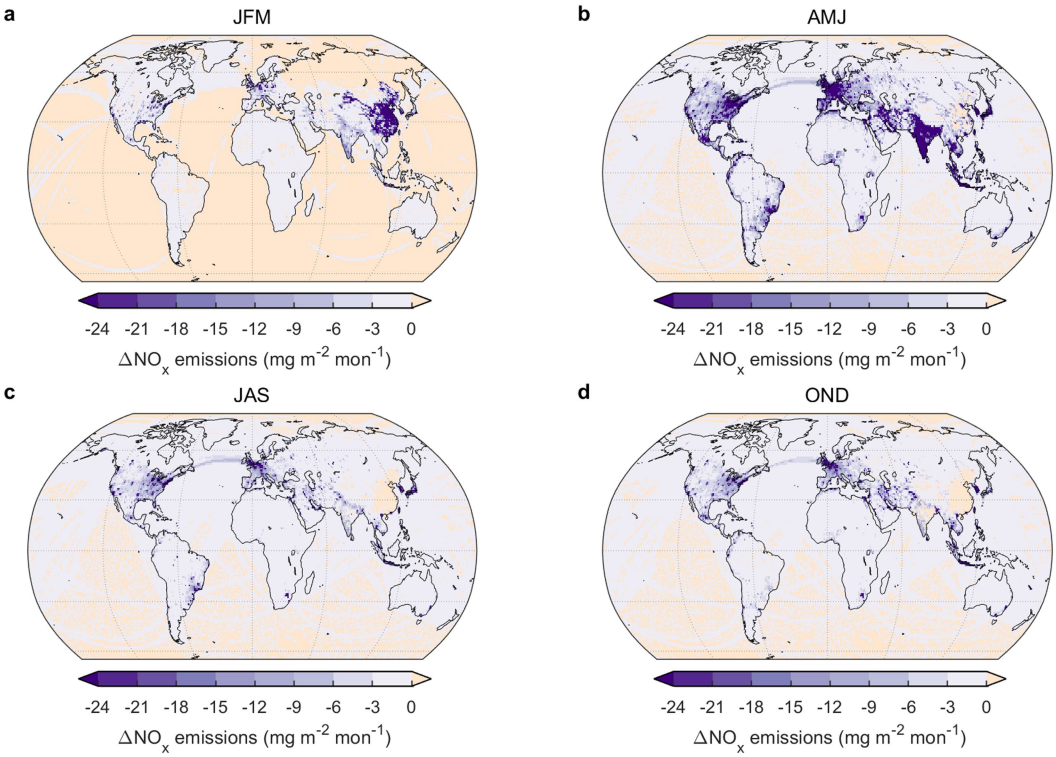

Extended Data Fig. 6 | Spatial patterns of difference in seasonal NO_x emissions between 2020 and 2019. a–d, JFM, AMJ, JAS and OND indicate the three consecutive months from January to December. The CEDS emissions data are available at https://data.pnnl.gov/dataset/CEDS-4-21-21.

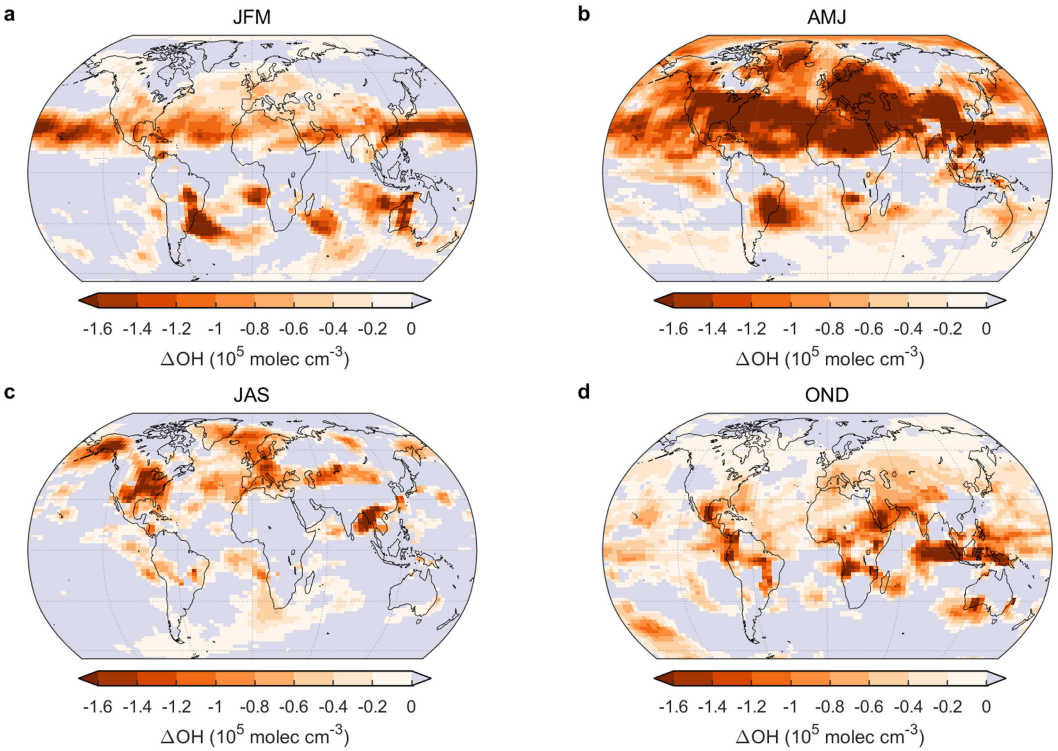

Extended Data Fig. 7 | Spatial patterns of difference in seasonal tropospheric OH concentration between 2020 and 2019. a–d, The OH field is simulated by a full chemistry transport model (LMDz-INCA) prescribed with CO and NO_x emissions derived from gridded near-real-time fossil fuel combustion data (see Methods). JFM, AMJ, JAS and OND indicate the three consecutive months from January to December.

nature portfolio

Corresponding author(s): Shushi Peng, Xin Lin

Last updated by author(s): Sep 15, 2022

Reporting Summary

Nature Portfolio wishes to improve the reproducibility of the work that we publish. This form provides structure for consistency and transparency in reporting. For further information on Nature Portfolio policies, see our Editorial Policies and the Editorial Policy Checklist.

Statistics

For all statistical analyses, confirm that the following items are present in the figure legend, table legend, main text, or Methods section.

n/a	Confirmed	
☐	☒	The exact sample size (*n*) for each experimental group/condition, given as a discrete number and unit of measurement
☒	☐	A statement on whether measurements were taken from distinct samples or whether the same sample was measured repeatedly
☐	☒	The statistical test(s) used AND whether they are one- or two-sided *Only common tests should be described solely by name; describe more complex techniques in the Methods section.*
☒	☐	A description of all covariates tested
☒	☐	A description of any assumptions or corrections, such as tests of normality and adjustment for multiple comparisons
☐	☒	A full description of the statistical parameters including central tendency (e.g. means) or other basic estimates (e.g. regression coefficient) AND variation (e.g. standard deviation) or associated estimates of uncertainty (e.g. confidence intervals)
☐	☒	For null hypothesis testing, the test statistic (e.g. *F*, *t*, *r*) with confidence intervals, effect sizes, degrees of freedom and *P* value noted *Give P values as exact values whenever suitable.*
☒	☐	For Bayesian analysis, information on the choice of priors and Markov chain Monte Carlo settings
☒	☐	For hierarchical and complex designs, identification of the appropriate level for tests and full reporting of outcomes
☒	☐	Estimates of effect sizes (e.g. Cohen's *d*, Pearson's *r*), indicating how they were calculated

Our web collection on statistics for biologists contains articles on many of the points above.

Software and code

Policy information about availability of computer code

Data collection	Atmospheric methane concentration observations at surface sites, by aircraft campaigns and by satellites, climate data, fire emissions, anthropogenic methane emissions, NOx emissions, activity data for anthropogenic methane emissions, and satellite observed atmospheric NO2 concentration, as well as input data for models are downloaded from publicly available websites. Please see the section "Data availability".
Data analysis	Code and documentation for ORCHIDEE (MICT v8.4.4) is publicly available at http://forge.ipsl.jussieu.fr/orchidee/. Code and documentation for the LPJ-wsl model is publicly available at https://github.com/benpoulter/LPJ-wsl_v2.0.git. The LMDZ-INCA global model is part of the Institut Pierre Simon Laplace (IPSL) Climate Modelling Center Coupled Model. The documentation on the code and the code itself can be found at https://cmc.ipsl.fr/ipsl-climate-models/ipsl-cm6/. Model outputs were processed using the software MATLAB R2021a.

For manuscripts utilizing custom algorithms or software that are central to the research but not yet described in published literature, software must be made available to editors and reviewers. We strongly encourage code deposition in a community repository (e.g. GitHub). See the Nature Portfolio guidelines for submitting code & software for further information.

Data

Policy information about availability of data

All manuscripts must include a data availability statement. This statement should provide the following information, where applicable:

- Accession codes, unique identifiers, or web links for publicly available datasets
- A description of any restrictions on data availability
- For clinical datasets or third party data, please ensure that the statement adheres to our policy

All observation and model data that support the findings of this study are available as follows. The atmospheric methane growth rate data are obtained from https://gml.noaa.gov/ccgg/trends_ch4/. The GOSAT satellite data are obtained from https://data2.gosat.nies.go.jp/GosatDataArchiveService/usr/download/DownloadPage/view. The EDGAR v6.0 data are downloaded from https://edgar.jrc.ec.europa.eu/country_profile. The hourly ERA5 reanalysis data are downloaded from https://www.ecmwf.int/en/forecasts/dataset/ecmwf-reanalysis-v5. The monthly precipitation data from MERRA2 are downloaded from https://gmao.gsfc.nasa.gov/reanalysis/MERRA-2/. The monthly temperature and precipitation data from CRU TS v4.05 are downloaded from https://crudata.uea.ac.uk/cru/data/hrg/cru_ts_4.05/. The monthly precipitation from MSWEP v2.8 are downloaded from http://www.gloh2o.org/mswep/. The GLEAM v3.5a root-zone soil moisture data are downloaded from https://www.gleam.eu/. The RFW data sets are available at https://doi.pangaea.de/10.1594/PANGAEA.892657. The land liquid water equilibrium from the GRACE-FO satellite are downloaded from https://gracefo.jpl.nasa.gov/data/grace-fo-data/. The Global Fire Emissions Database version 4.1 including small fire burned area are obtained from https://www.geo.vu.nl/~gwerf/GFED/GFED4/. The monthly global fire methane emissions from the Global Fire Assimilation System (GFAS) from Copernicus Atmosphere Monitoring Service (CAMS) are obtained from https://apps.ecmwf.int/datasets/data/cams-gfas/. The anthropogenic emissions from the CEDS emission inventory up to 2019 are downloaded from https://data.pnnl.gov/dataset/CEDS-4-21-21. The gridded near-real time fossil fuel combustion data that include confinement induced reductions in 2020 are obtained https://carbonmonitor.org/. The tropospheric NO2 concentration data from OMI satellite measurements are downloaded from https://disc.gsfc.nasa.gov/datasets/OMNO2_003/summary. The NOAA and ICOS surface CH4 observations used in inversions are available at https://doi.org/10.15138/VNCZ-M766 and https://doi.org/10.18160/KCYX-HA35, respectively; surface CH4 observations from other networks are available from World Data Centre for Greenhouse Gases (https://gaw.kishou.go.jp/) and Global Environmental Database (https://db.cger.nies.go.jp/ged/en/index.html). The TCCON XCH4 data are obtained from the TCCON Data Archive hosted by CaltechDATA at https://tccondata.org. The aircraft CH4 vertical profiles are from NOAA's GGGRN (available at https://gml.noaa.gov/ccgg/obspack/), IAGOS (available at https://www.iagos.org/) and JMA (available at https://gaw.kishou.go.jp/). The CH4 measurements from NOAA's AirCore compaigns are publicly available at https://gml.noaa.gov/aftp/data/AirCore/. The outputs of the two WEMs, LMDZ-INCA and atmospheric 3D inversions are publicly available at Figshare (doi: 10.6084/m9.figshare.21076171).

Human research participants

Policy information about studies involving human research participants and Sex and Gender in Research.

Reporting on sex and gender	*Use the terms sex (biological attribute) and gender (shaped by social and cultural circumstances) carefully in order to avoid confusing both terms. Indicate if findings apply to only one sex or gender; describe whether sex and gender were considered in study design whether sex and/or gender was determined based on self-reporting or assigned and methods used. Provide in the source data disaggregated sex and gender data where this information has been collected, and consent has been obtained for sharing of individual-level data; provide overall numbers in this Reporting Summary. Please state if this information has not been collected. Report sex- and gender-based analyses where performed, justify reasons for lack of sex- and gender-based analysis.*
Population characteristics	*Describe the covariate-relevant population characteristics of the human research participants (e.g. age, genotypic information, past and current diagnosis and treatment categories). If you filled out the behavioural & social sciences study design questions and have nothing to add here, write "See above."*
Recruitment	*Describe how participants were recruited. Outline any potential self-selection bias or other biases that may be present and how these are likely to impact results.*
Ethics oversight	*Identify the organization(s) that approved the study protocol.*

Note that full information on the approval of the study protocol must also be provided in the manuscript.

Field-specific reporting

Please select the one below that is the best fit for your research. If you are not sure, read the appropriate sections before making your selection.

☐ Life sciences ☐ Behavioural & social sciences ☒ Ecological, evolutionary & environmental sciences

For a reference copy of the document with all sections, see nature.com/documents/nr-reporting-summary-flat.pdf

Ecological, evolutionary & environmental sciences study design

All studies must disclose on these points even when the disclosure is negative.

Study description	The study explains why an unexpected very high atmospheric methane growth rate — the highest value from 1984 to 2020, happened in 2020, although COVID-19 confinements could likely decrease anthropogenic methane emissions. To answer this question, we did a comprehensive synthesis for global methane budget in 2020 compared to 2019, combining both bottom-up and

	top-down methods. We find that both higher wetland emissions due to warmer and wetter climate and lower atmospheric methane sink — from decreased hydroxyl radical (OH) concentration due to lower anthropogenic NOx emissions during the confinements in 2020 relative to 2019, explain why methane soared in the atmosphere in 2020.
Research sample	This is a synthesis of global methane budget in 2020 compared to 2019, combining bottom-up and top-down methods. For the bottom-up methods, we estimated methane emissions including anthropogenic, fire and wetlands sources. We also provided simple estimates for changes in emissions from lakes (including reservoirs) and permafrost between 2020 and 2019. For the top-down methods, first, we estimated tropospheric OH by two independent methods (a full chemistry transport model and a box-model with three fluorinated gases as new tracers), and then prescribed the OH from the full chemistry transport model into a 3D atmospheric inversion to see the spatial distribution of methane sources and sink anomalies in 2020.
Sampling strategy	N/A
Data collection	Atmospheric methane concentration observations at surface sites, by aircraft campaigns, and by satellites, climate data, fire emissions, anthropogenic methane emissions, NOx emissions, activity data for anthropogenic methane emissions, and satellite observed atmospheric NO2 concentration, as well as input data for models are downloaded from publicly available websites (Please see section "data availability").
Timing and spatial scale	This study mainly focuses on global methane budget in 2020 relative to 2019. The bottom-up methods cover global scale and the period 2000-2020. The top-down method covers global scale and the period 2015-2020.
Data exclusions	N/A
Reproducibility	This study was based on publicly available data and well-defined models/methods, and could be reliably reproduced.
Randomization	N/A
Blinding	N/A

Did the study involve field work? ☐ Yes ☒ No

Reporting for specific materials, systems and methods

We require information from authors about some types of materials, experimental systems and methods used in many studies. Here, indicate whether each material, system or method listed is relevant to your study. If you are not sure if a list item applies to your research, read the appropriate section before selecting a response.

Materials & experimental systems

n/a	Involved in the study
☒	☐ Antibodies
☒	☐ Eukaryotic cell lines
☒	☐ Palaeontology and archaeology
☒	☐ Animals and other organisms
☒	☐ Clinical data
☒	☐ Dual use research of concern

Methods

n/a	Involved in the study
☒	☐ ChIP-seq
☒	☐ Flow cytometry
☒	☐ MRI-based neuroimaging